In Situ Single-Molecule Imaging with Attoliter Detection Using Objective Total Internal Reflection Confocal Microscopy†

Thomas P. Burghardt,*,‡ Katalin Ajtai,‡ and Julian Borejdo§

Department of Physiology and Biomedical Imaging, Mayo Clinic, Rochester, Minnesota 55905, and Department of Molecular Biology and Immunology, University of North Texas HSC, Fort Worth, Texas 76107

Received October 14, 2005; Revised Manuscript Received February 2, 2006

ABSTRACT: Confocal microscopy is widely used for acquiring high spatial resolution tissue sample images of interesting fluorescent molecules inside cells. The fluorescent molecules are often tagged proteins participating in a biological function. The high spatial resolution of confocal microscopy compared to wide field imaging comes from an ability to optically isolate and image exceedingly small volume elements made up of the lateral (focal plane) and depth dimensions. Confocal microscopy at the optical diffraction limit images volumes on the order of ∼0.5 femtoliter (10^{-15} L). Further resolution enhancement can be achieved with total internal reflection microscopy (TIRM). With TIRM, an exponentially decaying electromagnetic field (near-field) established on the surface of the sample defines a subdiffraction limit dimension that, when combined with conventional confocal microscopy, permits image formation from <7 attoL (10^{-18} L) volumes [Borejdo et al. (2006) *Biochim. Biophys. Acta*, in press]. Demonstrated here is a new variation of TIRM, focused TIRM (fTIRM) that decreases the volume element to ∼3 attoL. These estimates were verified experimentally by measuring characteristic times for Brownian motion of fluorescent nanospheres through the volume elements. A novel application for TIRM is in situ single-molecule fluorescence spectroscopy. Single-molecule studies of protein structure and function are well-known to avoid the ambiguities introduced by ensemble averaging. In situ, proteins are subjected to the native forces of the crowded environment in the cell that are not present in vitro. The attoL fluorescence detection volume of TIRM permits isolation of single proteins in situ. Muscle tissue contains myosin at a ∼120 μM concentration. Evidence is provided that >75% of the bleachable fluorescence detected with fTIRM is emitted by five chromophore-labeled myosins in a muscle fiber.

Protein structure and function is widely studied using tools designed to isolate and characterize single molecules. The approach avoids certain ambiguities introduced by ensemble averaging, thereby providing substantially more insight into protein dynamics accompanying function (*1*, *2*). Motor proteins operating on the substrate in vitro is an example of a system successfully investigated with the single-molecule approach (*3*, *4*). While the approach is advantageous in many ways, single molecules in vitro do not fully exemplify the native system in a cell where molecular crowding is the norm (*5*, *6*). A crowded environment potentially affects protein solubility, structure, and kinetics, suggesting that proteins in situ function differently from their in vitro counterpart. For instance, the crowded environment is known to produce preferential hydration of a target protein favoring lower surface area structures and promoting self-association. Single-molecule studies conducted in situ are clearly preferable when feasible.

An interesting target protein subjected to molecular crowding is the motor protein myosin in muscle. In the skeletal muscle sarcomere, myosin forms thick filaments interdigitated with polymerized actin thin filaments. The filaments produce contraction by a relative sliding movement accompanied by myosin hydrolysis of ATP and sarcomere shortening (*7*, *8*). Thick filaments are concentrated into the sarcomeric A-band where the myosin concentration is estimated to be ∼120 μM (*9*), implying ∼72 myosins per attoL (10^{-18} L). Using fluorescence detection of an extrinsic chromophore specifically labeling ∼1% of the myosin molecules, ∼1.4 attoL observation volume is needed to isolate a fluorescent signal from a single sarcomeric myosin. AttoL volume resolution is beyond diffraction-limited optics, stimulating wide interest in alternative approaches to relax diffraction-limited constraints.

The standard optical microscope employs a propagating field (or far-field) electromagnetic radiation for imaging and is a diffraction-limited instrument; however, there are some notable exceptions. Schrader et al. (*10*) demonstrated subdiffraction resolution using a 4Pi microscope with two-photon excitation. Coherent light, focused through two high-aperture objectives subtending a large solid angle about the sample, constructively interferes at the focus to produce an intensity peak much narrower than that obtainable from a

† Supported by NIH−NIAMS Grant R01AR049277 and the Mayo Foundation (to T.P.B. and K.A.) and by R21CA9732 and R01AR048622 (NIAMS) (to J.B.).

* To whom correspondence should be addressed. Telephone: 507-284-8120. Fax: 507-284-9349. E-mail: burghardt@mayo.edu.

‡ Mayo Clinic.

§ University of North Texas HSC.

10.1021/bi052097d CCC: $33.50
Published on Web 03/09/2006

single objective but at the cost of additional side lobes displaced laterally from the focus. The confocal pinhole plus image processing effectively removes the side lobe contributions. They demonstrated a resolution on the order of 100 nm in three dimensions, corresponding to a detection volume probably somewhat larger than 1 attoL. Klar et al. (*11*) demonstrated a 0.67 attoL fluorescence detection volume in a far-field microscope using stimulated emission depletion (STED). Synchronized probing and STED laser beams excite fluorescence in a normal diffraction-limited volume and then quench fluorescence from the periphery of a volume using stimulated emission initiated by the STED beam that is red-shifted from the probing beam. The intensity profile of the STED beam is controlled to engineer shape and size of the volume from which fluorescence is detected. A microscope using STED or a related depletion technique appears able to shrink the detected fluorescent volume size without limit. Recently, the 4Pi and STED technologies were combined to achieve an axial resolution of ~50 nm (*12*).

Near-field microscopes make use of a nonpropagating evanescent field that decays exponentially in space to define a subdiffraction-limited volume. Near-field scanning optical microscopy (NSOM) probes (*2*) and zero-mode waveguides (*13*, *14*) squeeze light through a nanoscale aperture to produce an evanescent field confined to the immediate vicinity of the aperture. NSOM makes use of a tapered fiber optic tip scanned over the sample to produce subdiffraction-limited resolution images of the surface. Zero-mode waveguides are not scanned, but they define a tiny illuminated volume on the sample surface. Either near-field method produces detection volumes of ~1 attoL

Total internal reflection microscopy (TIRM)[1] produces an evanescent field on the water side of the glass/water interface made by a coverslip contacting aqueous solution (*15*). Excitation is delivered through the glass side by propagating light incident on the interface at angles beyond the critical angle for total internal reflection (*16*). Prism and prismless forms of TIRM have been described (*17*). Prismless TIRM utilizes a high numerical aperture oil immersion objective to refract excitation laser light at supercritical angles for total internal reflection (*18*). The evanescent field decays exponentially in the direction normal to the interface. Usually, prismless TIRM is setup to illuminate a uniform field in object space (unfocused TIRM or uTIRM) using a laser beam focused at the back focal plane. Ruckstuhl and Seeger (*19*−*21*) developed prismless TIRM with a parabolic mirror objective (PMO) producing a focused spot on the sample in the aqueous medium (focused TIRM or fTIRM). They combined fTIRM with confocal microscopy and investigated dye diffusion characteristics with fluorescence correlation spectroscopy (*22*). The findings indicated that the detection volume produced with this setup is <5 attoL. The instrument described here resembles Ruckstuhl and Seeger's but where a conventional high aperture objective substitutes for the PMO. We demonstrate with diffusing fluorescent nanospheres that the instrument produces a detection volume of ~3 attoL. This development permits attoL volume illumination with off-the-shelf microscope components.

[1] Abbreviations: u(f)TIRM, (un)focused total internal reflection microscopy.

The myosin motor in a skeletal muscle fiber can be specifically modified by a fluorescent probe. Modification can be covalent where a derivative of tetramethylrhodamine specifically reacts with the fast-reacting thiol (SH1 or Cys707) in the myosin catalytic domain (*23*). We have shown that a confocal microscope equipped with uTIRM isolates individual SH1-modified or light-chain-labeled myosin motors in myofibrils, thus accomplishing an important first step toward in situ single-molecule studies in muscle (*24*). The new variation of fTIRM introduced here has the advantages of uTIRM but with a significantly smaller detection volume.

MATERIALS AND METHODS

Chemicals. Carboxylate-modified fluorescent microspheres and 5′-iodoacetamidotetramethylrhodamine (5′-IATR) were purchased from Molecular Probes (Eugene, OR). ATP, dithiothreitol (DTT), Triton ×100, and phenylmethanesulfonyl fluoride (PMSF) were from Sigma Chemical (St. Louis, MO). All chemicals are analytical-grade.

Solutions. Rigor solution contains 80 mM KCl, 5 mM $MgCl_2$, 2 mM ethylene glycol bis(β-aminoethyl ether)-*N*,*N*,*N*′,*N*′-tetraacetic acid (EGTA), 1 mM DTT, 0.2 mM PMSF, and 5 mM phosphate buffer. Relaxing solution is rigor solution plus 4 mM ATP. Glycerinating solution is relaxing solution with 50% glycerol (volume/volume). Skinning solution is relaxing solution containing 0.5% Triton ×100. Labeling solution is relaxing solution without DTT. All solutions are pH 7.

Fluorescent Spheres. Nile red and orange carboxylate-modified fluorescent spheres had 20 and 100 nm diameters and excitation/emission maxima at 535/575 and 540/560 nm according to the Molecular Probes catalog. Sphere fluorescence was observed with a rhodamine filter set. Sphere concentrations were computed using the formula in the catalog after dilution in rigor buffer. We used 10^4- and 10^3-fold dilutions from stock, giving sphere concentrations of 4.5×10^{11} and 3.6×10^{10} spheres/mL for the 20 and 100 nm spheres, respectively. All experiments were conducted at room temperature.

Coverslip Cleaning and Sample Chamber Preparation. Clean glass or suprasil quartz (Chemglass, Vineland, NJ) #1 coverslips were sonicated for 10 min in ethanol and then plasma-cleaned (Harrick Plasma, Ithaca, NY) for 15−30 min. Plasma cleaned coverslips were placed on a 1″ × 3″ brass slide with a large hole cut out, permitting the objective from the inverted microscope to contact the coverslip through immersion oil. A water-tight chamber was constructed on top of the plasma-cleaned coverslip as shown in Figure 1. The chamber top was formed by another #1 thickness coverslip made shorter than the bottom coverslip by slicing off two 2 mm wide rectangles of glass using a diamond-tipped pen. Two opposing sides of the chamber were formed by narrow silicon grease stripes extruded from a pipet tip at about the thickness of the coverslip. The grease stripes ran the length of the bottom coverslip and defined a 3−5 mm wide band through the center. The other opposing sides of the chamber were left open, allowing input and output of solutions to the chamber. The rectangular glass slices cut from the top coverslip were placed on the outer edges of the plasma-cleaned slide to act as spacers between the chamber top and bottom. In the figure spacers are shown

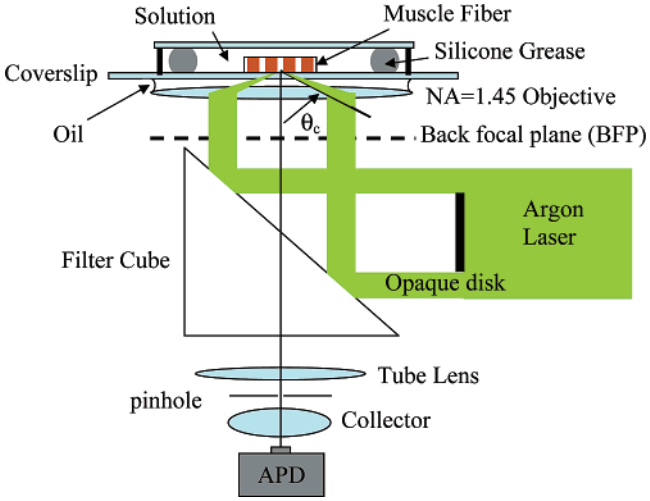

FIGURE 1: fTIRM optical setup. Excitation light from the expanded laser beam is partially blocked by the opaque disk to form an annulus of light reflected by the filter cube and illuminating the objective BFP. Light is refracted at the objective to form a focused spot on the glass/coverslip interface. All refracted light is incident on the interface at angles beyond the critical angle for total internal reflection. The evanescent light at the interface excites fluorescence in the sample surface that is collected by the objective. Fluorescence transmits the filter cube and is focused by the tube lens on the pinhole. A collector lens focuses light transmitting the pinhole onto the active surface of the APD.

taller for clarity. The chamber may contain a muscle fiber (as shown) or a suspension of nanospheres.

Muscle-Fiber Preparation and Modification with a Fluorescent Probe. Rabbit *psoas* muscle fibers were obtained as previously described (*25*) and kept in glycerinating solution at −15 °C for up to several weeks. All fiber preparations were performed at 4 °C. In the standard fiber-labeling procedure, muscle fibers are bathed in skinning solution (10 min) to remove the membrane and then placed in labeling solution containing 70 μM 5′-IATR for 30 min. The labeling reaction is stopped with 1 mM DTT and excess dye exhaustively washed out with relaxing solution (2 h) (*23*). Under these circumstances, we showed that 77−86% of the total probe intensity emitted from the 5′-IATR label in modified fibers originates from the myosin heavy-chain reactive thiol (SH1 or Cys707) (*26*). Myosin extracted from the labeled fibers had ∼0.32 probe/myosin headgroup (*27*). Fibers labeled to this degree exhibited a normal isometric tension of ∼172 ± 50 kN/m^2. In experiments described here, we used fibers labeled by a modified protocol. The modified protocol is identical to the standard one except that the labeling solution contained 10 μM 5′-IATR and the incubation time was shortened to 20 min. We expect the labeling efficiency to be significantly decreased without the loss of specificity.

Microscope fluorescence measurements on muscle fibers were performed at 20 °C.

Confocal fTIRM. Figure 1 shows the fTIRM instrument diagram. Plane polarized light from an expanded argon ion laser beam impinges on an opaque annular disk. The disk restricts light to the annular region that, when refracted by the NA 1.45 60× oil immersion objective (Olympus, Melville, NY), propagates toward the coverslip at angles greater than the critical angle, $\theta_c \approx 63°$. A fluorescent-labeled muscle fiber in aqueous buffer solution makes contact with the coverslip at the focused spot and is illuminated by the evanescent field. Excited fluorescence collected by the objective is filtered and formed into an image by the tube lens at the confocal pinhole aperture. The collector lens focuses divergent fluorescent light, transmitting the pinhole onto the avalanche photodiode (APD) detector.

The APD outputs a TTL-compatible pulse for each detected photon. A counter/timer card (6602, National Instruments, Austin, TX) counts pulses over time bins ≥4 μs. Custom-written programs in Labview software control the counter/timer card and display/process data.

In some experiments, we utilized uTIRM illumination. The annular disk in Figure 1 was replaced by a lens that focuses excitation light at the back focal plane (BFP). The lens is displaced in the plane perpendicular to the beam propagation direction until the focused spot at the BFP lies outside the shadow created by the opaque disk when present (*18*).

Sphere Diffusion through the Detected Volume. Fluorescent spheres in Brownian motion translate through the detected volume, producing time-dependent fluorescence intensity. Fluorescence intensity depends upon sphere diffusion constant D, detection volume (V_d) size and shape, and constraints imposed on the sphere position by the presence of the planar glass/water interface, where total internal reflection occurs. We model sphere diffusion as a three-dimensional random walk subject to constraints imposed by the presence of the planar interface, compute the time-dependent fluorescence intensity, and compare computed with observed signals to deduce the size and shape of V_d.

A sphere, the solute, undergoing a random walk in one dimension moves a step of length, δ, in each time interval, τ. Displacement of the solute after n steps is $x = (n - 2n_-)\delta$, where n_- is the number of steps in the $-x$ direction. It can be shown by statistical arguments that the ensemble averaged displacement squared $\langle x^2 \rangle = n\delta^2$ (*28*). Generalized to three dimensions, $\langle r^2 \rangle = 3n\delta^2$, where r is the radial distance from the starting point. In time $t = n\tau$ and for a diffusion constant $2D\tau = \delta^2$, we get the Sutherland−Einstein diffusion equation

$$\langle r^2 \rangle = 3n\delta^2 = 6Dt \qquad (1)$$

Step length δ is the solute mean free path between collisions with the solvent. The distance between water molecules at a 55 M concentration suggests $\delta \sim 3 \times 10^{-4}$ μm, implying from eq 1 that the number of steps needed to move about 1 μm is ∼10^7. Simulations using 3×10^{-4} μm step sizes were not tractable. Choosing a longer step will not change anything in the problem provided that we also lengthen the step time τ and do not seek to characterize the particle movement in time segments $\lesssim 10\tau$. The Einstein−Smoluchowski relation gives the diffusion constant, $D = kT/(6\pi s_r \eta)$, where kT is the thermal energy, s_r is the sphere radius, and η is the fluid viscosity. The diffusion constants for the 20 and 100 nm spheres in water at room temperature are 2.2×10^{-7} and 4.4×10^{-8} cm^2/s, respectively. A $\delta = 2$ nm step size is 10-fold smaller than any linear dimension in our system and should be small enough to accurately account for solute diffusion in the system. For this δ, we obtain $\tau = 0.02$ μs, a characteristic time 200-fold shorter than any time-dependent measurement that we can make. The real sphere executes

multiple random steps for each simulated step; however, the dimensions of the system and the time frame of our measurements prohibit any detectable effect from this computational short cut.

Three vectors, v_x, v_y, and v_z of dimension N [$v_i(j)$, $j = 1, ..., N$] were constructed from the randomly chosen integers -1 or 1 corresponding to $-$ or $+$ direction steps. The three vectors assigned to the *x*-, *y*-, and *z*-spatial dimensions determine the spatial path of the sphere center as a function of the step number $\{x_S(n), y_S(n), z_S(n)\} = \sum_{j=1,n}\delta\{v_x(j), v_y(j), v_z(j)\}$, for $n \leq N$. The step number converts to time with $t = n\tau$ (the time it takes to complete n steps) and $\tau = D/(2\delta^2)$. A sphere is detected when any part of it intersects V_d, hence the midpoint of each sphere path (where $t = \tau n/2$) is translated to a randomly chosen point within V_d and the entire length of the path is traced to see if any part of the sphere intersects the planar surface where TIR occurs. If the sphere and surface collide, the path is rejected. We typically collected 40−100 sphere paths for an ensemble.

In practice, spheres collide with the surface on pathways included in the experimental ensemble, inviting the question of how relevant the simulation is to the experiment. Allowed sphere positions occur on a lattice defined by step size δ and starting from $z = \delta$, with the TIR planar surface at $z = 0$. Just before collision, the sphere resides at $z = \delta$. At step n, it moves in the $-z$ direction, colliding with the surface, reversing direction, and then stopping at $z = 2\delta$. Position $z = 2\delta$ is the place that the sphere would have occupied if it had taken step n in the $+z$ direction (a sphere never remains in the same place in any dimension after a step). The latter path is one that we include in our ensemble in the collision-rejecting method, implying that we find every path that the sphere can take in the presence of the surface. Evidentially, a path involving collisions can also be created without collisions, suggesting that path frequency is under-represented in the collision-rejecting method. However, path degrees of freedom are so large there is negligible probability that one path will ever be repeated. Thus, rejecting sphere paths that collide with the surface is an appropriate strategy to include the surface effect on trajectory without explicitly treating the collision process.

The detected fluorescence intensity is proportional to sphere surface area (or volume, depending upon how chromophores are distributed within the sphere) falling within V_d. The quantity is computed for each point in the sphere path. Sphere size and its diffusion constant are known leaving V_d, defined by the electric field spatial distribution and the pinhole aperture (see *Size and Shape of V_d*), the only unknown.

The fluorescence signal from the diffusing sphere will be mainly a null signal disturbed occasionally by short fluorescence bursts when the sphere enters and then leaves V_d (possibly several times in one encounter). The number-residence duration distribution, $R_n(t,V_d)$, characterizes the sphere residence in V_d. It is the number of t duration events produced by an ensemble of sphere paths as a function of t. The encounter of a single sphere with V_d will produce one or several events contributing to $R_n(t,V_d)$. The many sphere paths in an ensemble will produce similar contributions. From $R_n(t,V_d)$, we compute the mean residence time $\langle t\rangle_n$ and root-mean-squared (rms) deviation of the residence time $(\langle\Delta t^2\rangle_n)^{1/2} = (\langle(t - \langle t\rangle)^2\rangle_n)^{1/2}$, given by

$$\langle t\rangle_n = \frac{\sum_k (k\cdot\delta t)R_n(k\cdot\delta t,V_d)}{\sum_k R_n(k\cdot\delta t,V_d)}$$

$$\langle(\Delta t)^2\rangle_n + \langle t\rangle_n^{\,2} = \frac{\sum_k (k\cdot\delta t)^2 R_n(k\cdot\delta t,V_d)}{\sum_k R_n(k\cdot\delta t,V_d)} \qquad (2)$$

where k is summed over recorded events and δt is the sampling interval. Potentially more pertinent to fluorescence detected events is the fluorescence-intensity-residence duration distribution, $R_f(t,V_d)$, computed like R_n, except that summed fluorescence intensity during an event, rather than the number of events, of t duration is the distribution amplitude. Mean and rms deviation residence times from $R_f(t,V_d)$, $\langle t\rangle_f$, and $(\langle\Delta t^2\rangle_f)^{1/2}$ are computed using eq 2 with R_f replacing R_n.

Mean and rms deviation residence times will depend to some extent upon δt because sphere movement near the edges of V_d will produce detectable events for short δt that will go undetected for long δt (see *Event Detection*). We remove inconsistencies caused by this effect by using two sampling times exclusively, 5 and 50 μs, for experiments and simulations on the 20 and 100 nm spheres, respectively.

Photon Statistics. The sphere concentration is low enough that only one sphere is inside V_d at a time. Illumination of a solution containing fluorescent spheres will produce fluorescence intensity $f(t)$ at the detector (not including statistical effects) given by

$$f(t) - f_b(t) \propto \int C_p(x - x_S(t), y - y_S(t), z - z_S(t))\mathrm{IPSF}(x,y,z)\mathrm{d}x\mathrm{d}y\mathrm{d}z = P(t) \qquad (3)$$

where $f_b(t)$ is the background, C_p is the probe density (finite and constant within the sphere and 0 otherwise), the sphere center coordinates$\{x_S(t), y_S(t), z_S(t)\}$ that move as the sphere diffuses, and IPSF(x,y,z) is the integrated point spread function (see *Size and Shape of V_d*). $P(t)$ represents the overlap of the sphere volume with V_d at time t and corresponds to a particular number of fluorescing probes. The fluorescing probes give rise to an intensity at the detector with photon count distribution $p(k,\langle k\rangle,\epsilon)$ for k photons/sampling interval, with the expectation value $\langle k\rangle = \alpha P(t)$ and parameter ϵ related to a real detector correction as discussed below. Proportionality constant α relates photons detected to photons emitted for a particular microscope and sampling time interval. The background light has an identical photon count distribution but stationary expectation value $\langle k\rangle = \langle k\rangle_b$. Hence, the total photon count distribution, $p_T(k,t,\epsilon)$, including the background and sample counts is

$$p_T(k,t,\epsilon) = p(k,\langle k\rangle_b,\epsilon) + p(k,\langle k\rangle = \alpha P(t),\epsilon) \qquad (4)$$

Equation 4 is evaluated for a stochastic process by generating random photon counts with the distribution $p(k,\langle k\rangle,\epsilon)$. For an ideal detector, $p(k,\langle k\rangle,\epsilon)$ is a Poisson distribution. Real detector after-pulsing probability, θ_a, and dead time, t_d, modify $p(k,\langle k\rangle,\epsilon)$ as discussed by Hillesheim and Müller (*29*).

After-pulsing probability is small ($\theta_a < 0.003$), and to first order modifies the ensemble average photon number $\langle k\rangle \rightarrow (1 + \theta_a)\langle k\rangle$. For our application, this after-pulsing correction can be ignored throughout by using the observed $\langle k\rangle$ (as opposed to the real $\langle k\rangle$) when evaluating eq 4. A more significant effect (for us) is its apparent contribution to the higher than expected probability for two photons per counting time interval in the background. The prevalence of spurious two photon events required us to set a minimum two photon threshold for event detection (see *Event Detection*).

After a photon is detected, the dead time must pass before another photon hitting the APD will be registered. Finite dead time modifies the shape and position (in k) of the photon count distribution as a function of $\epsilon \equiv t_d/T_s$, where T_s is the sampling time interval. We used $p(k,\langle k\rangle,\epsilon)$ derived by Hillesheim and Müller for dead time $t_d = 31$ ns measured from the APD at the factory.

Event Detection. Continuous fluorescence time courses lasted 0.25−5 s for sampling time intervals of 5−100 μs. Usually, 1−2 sphere detection events occurred during the time course, and 100 time courses were collected for each condition. Subsets of the fluorescence time course between sphere detection events were identified and used to set the background mean photons/sampling interval, $\langle k\rangle_b$. The measurement of $\langle k\rangle_b$ implies that the background light contribution to the fluorescence signal is fully characterized (eq 4). The remaining unknowns in the fluorescence signal are α and $P(t)$ in the expression $\langle k\rangle = \alpha P(t)$ (eq 4). At any instant in time, the mean photon count from the sphere in V_d, $\langle k\rangle = \alpha P(t_0)$, depends upon the sphere location in V_d because the excitation field is spatially inhomogeneous, making the direct measurement of $\alpha P(t)$ impossible. We estimate $\alpha P(t)$ from the peak photon count distribution as described below and find that this information is sufficient to constrain the size and shape of V_d.

Dilute samples of diffusing and fluorescing spheres were observed under fTIRM and uTIRM. Residence times for a sphere in V_d were observed from experimental data consisting of the fluorescence time course as spheres moved through V_d. More than 10^5 sphere detection events under various conditions were recorded, necessitating the creation of software for automated event detection. All programs were written in Mathematica 5.1 (Wolfram Research, Champaign, IL).

Event threshold, k_d, is the smallest integer photons per sampling interval count that cannot be achieved by the background over the time course consisting of M intervals. The probability for collecting $\geq n$ photons/sampling interval because of the background is

$$g(n) = \sum_{i=n}^{\infty} p(i,\langle k\rangle_b,\epsilon) = 1 - \sum_{i=0}^{n-1} p(i,\langle k\rangle_b,\epsilon) \qquad (5)$$

From eq 5, k_d is defined by

$$M\, g(k_d) < 1 \qquad (6)$$

The interval where photons/sampling interval are $\geq k_d$ starts a sphere detection event. Event termination threshold, k_t, is the minimum photon count that background light can achieve with a probability $\leq 50\%$. It is given by solving for integer k_t in the equation

$$p(k_t,\langle k\rangle_b,\epsilon) \leq \frac{1}{2} \qquad (7)$$

Event duration is the number of sample times between initiation and termination.

Measured event duration depends explicitly upon $\langle k\rangle_b$ through eqs 6 and 7 and implicitly on $\alpha P(t)$ because light detection from a sphere in V_d must be bright enough to overcome the threshold. $\langle k\rangle_b$ is estimated from light levels between well-separated intensity spikes identified with a sphere passing through V_d. We could not devise a practical method to measure $\alpha P(t)$, except implicitly by requiring simulated data, constructed with eq 4 and then analyzed by the event detection software, to have an event peak height distribution comparable to the measured data. In the simulation, we estimate $\alpha P(t)$ as a random Poisson distributed number, with an average value adjusted to reproduce the observed peak height distribution.

Size and Shape of V_d. Fluorescent intensity at the image plane in the diffraction-limited, far-field microscope is the convolution of the excitation and emission intensity profiles (*30*). The light intensity profiles are derived from geometrical optics and given by the Fraunhofer diffraction patterns from a circular aperture (*16*). Detected fluorescence is the intensity at the image plane integrated over the confocal pinhole; thus, the size and shape of the detected volume, V_d, depends upon the excitation beam profile, diffraction of emitted light through the microscope optics, and the size and shape of the confocal pinhole.

In our application, the spatial distribution of the excitation field intensity for fTIRM or uTIRM is unconventional. In either excitation mode, the field intensity decays exponentially in the dimension (z) normal to the glass/water interface. Intensity depth z_d is given by

$$z_d = \frac{\lambda}{4\pi\sqrt{(n_g \sin\theta)^2 - n_w^2}} \qquad (8)$$

where n_g or n_w are the refractive indices in glass or water, θ is the incidence angle, and λ is excitation light wavelength in a vacuum. Field intensity spatial distribution in lateral dimensions differs between the uTIRM and fTIRM excitation modes. uTIRM is uniform, while fTIRM forms a focused spot computed using expressions derived in the Appendix. The point spread function integrated over the pinhole aperture in the image space (integrated PSF or IPSF) as a function of the point source position sets boundaries for V_d appropriate for a pointlike diffusing fluorescent sphere. Results for uTIRM and fTIRM are shown in Figures 2−4 for a NA 1.45, 60× objective.

Figure 2A shows the two-dimensional intensity distribution in the focal plane (xy) on the water side of the interface (containing the sample) in fTIRM. Plotted on the z axis is the light intensity. The incident light plane polarization is along x. The profile is asymmetrical with the wider and bimodal intensity distribution in the direction of the incident plane polarization. Figure 2B shows the intensity distribution along the x (■) and y axis (◆). The 1/e intensity half widths of the focused spot are ∼180 and ∼70 nm. The intensity distribution in the z dimension (▲) is exponentially decaying with a width of ∼100 nm. For a comparison, the intensity

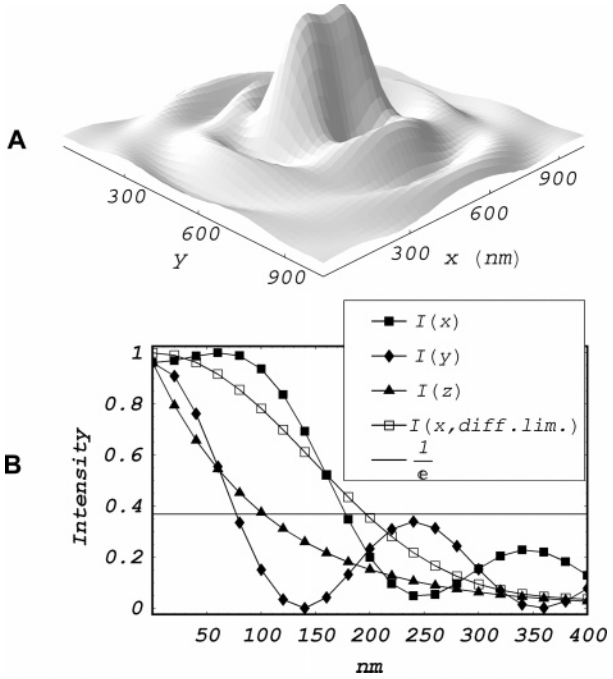

FIGURE 2: Light-intensity distribution of the evanescent field for TIRM. A is the light intensity in the focal plane ($z = 0$). The incident light plane polarization is along the x axis. B shows the intensity distribution along x (■, $1/e$ width ~180 nm) and y axes (◆, $1/e$ width ~70 nm). The intensity distribution in the z dimension (▲) is exponentially decaying with a width of ~100 nm. For a comparison, the intensity distribution along the x axis when the BFP is uniformly illuminated, i.e., a diffraction-limited spot, is also shown (□).

distribution along the x axis when the BFP is uniformly illuminated, i.e., a diffraction-limited spot, is also shown (□).

Figure 3A shows the IPSF for the intensity distribution in Figure 2 and a 10 μm pinhole as a function of the point source position near the focal plane (xy plane on the water side of the interface). Figure 3B is the IPSF under the same conditions as in Figure 3A but for the point source position in an axial plane (yz plane on the water side of the interface). The z-dimension dependence is exponential with a depth of field of ~100 nm. Parts A and B of Figure 3 show that the side lobe field intensities visible in Figure 2 are very effectively removed from the detection volume by the 10 μm pinhole. The 25 μm pinhole likewise effectively removes all side lobe field intensities from the IPSF, while the 50 μm pinhole admits the first-order side lobe intensities (data not shown). Parts C and D of Figure 3 are the IPSFs for uTIRM, 5 μm pinhole, and other conditions identical to that in parts A and B of Figure 3. A comparison of parts A and C of Figure 3 shows the narrowing of the IPSF because of focused excitation.

We used fTIRM for the isolation of single chromophores modifying myosin cross-bridges in muscle fibers. We calculate effective V_d for single-molecule isolation by deploying a rectangular solid lattice of identical chromophores in sample space. The lattice fills the volume occupied by the water and sample in a real experiment. A single chromophore in the lattice, the principal chromophore, occupies the sample space equivalent of the maximum intensity point in the IPSF (see Figure 3). Fluorescence detected from each chromophore in the lattice is summed and normalizes the fluorescence collected from the principal chromophore as a function of the unit-cell lattice dimensions. We define the minimum unit cell in the lattice to have dimensions for which the principal chromophore fluorescence accounts for more than half of the total fluorescence collected. The IPSFs shown in parts A and B and parts C and D of Figure 3 have a minimum unit cell with x, y, and z dimensions $L_x \times L_y \times L_z$ of 186 × 116 × 76 and 190 × 190 × 86 nm, respectively. The maximum volume defined by the lattice containing only the principal chromophore is the effective V_d. The IPSF shape suggests that it is the half ($z > 0$) triaxial ellipsoid centered on the origin with semi-axis lengths $L_x \times L_y \times L_z$ giving effective V_d values of ~3.4 and ~6.5 attoL.

Sensitivity of sphere diffusion characteristics to the shape and size of V_d was tested by computing the mean and rms deviation of residence times (eq 2) for a large variety of practical beam profiles. Table 1 summarizes the beam profiles considered and their V_d values. The diffraction-limited profile listed in Table 1 is a hypothetical construct made from combining the lateral profile from a diffraction-limited beam (when the BFP is fully illuminated as opposed to annular illumination, see Figure 1) with the axial profile of an evanescent field. Figure 4 shows the mean (■) and rms deviation (▲) for the number and fluorescence-intensity-residence duration distributions for 20 nm sphere-simulated diffusion. Correlation coefficients, ρ, of 0.98 or 0.96 between the rms deviation or mean fluorescence-intensity-residence duration and V_d, compared to 0.80 or 0.52 for their counterparts from the number-residence duration distribution, show that fluorescence-intensity-residence duration distribution is the more reliable indicator of V_d size.

The fluorescence residence duration distribution weighs heaviest events producing more fluorescence. Events produce more fluorescence when the single fluorescent sphere inside V_d traverses regions of higher excitation intensity closer to the TIR surface (at $z = 0$ in Figure 3) and centered laterally inside the focused spot. These spheres will also tend to spend more time inside V_d; thus, it is expected that fluorescence intensity weighting produces a parameter more sensitive to the V_d size.

The mean and rms deviations shown in Figure 4 are derived from simulated data without noise. When simulating real data, we include photon statistic effects (noise) contributed from the background and sphere fluorescence signals. On noisy data, we employ event detection (see *Event Detection*) to distinguish noise fluctuations from sphere detection events, leading to a dramatic decline in the mean and rms deviation of sphere residence duration in V_d. This is expected because points in the time-dependent fluorescence trace where the sphere is resident in V_d but near the edges of the volume where it produces lower fluorescence are indistinguishable from points where the sphere lies outside V_d. Ambiguous points are counted as times when the sphere lies outside V_d.

RESULTS

The top panel in Figure 5 shows fluorescence photon counts from a 20 nm diameter fluorescent sphere diffusing through $V_d \approx 3$ attoL for fTIRM illumination with a NA 1.45, 60× objective and 10 μm diameter confocal pinhole. Fluorescence collection sampling times were 5 μs. The bottom panel shows simulated data from a randomly walking

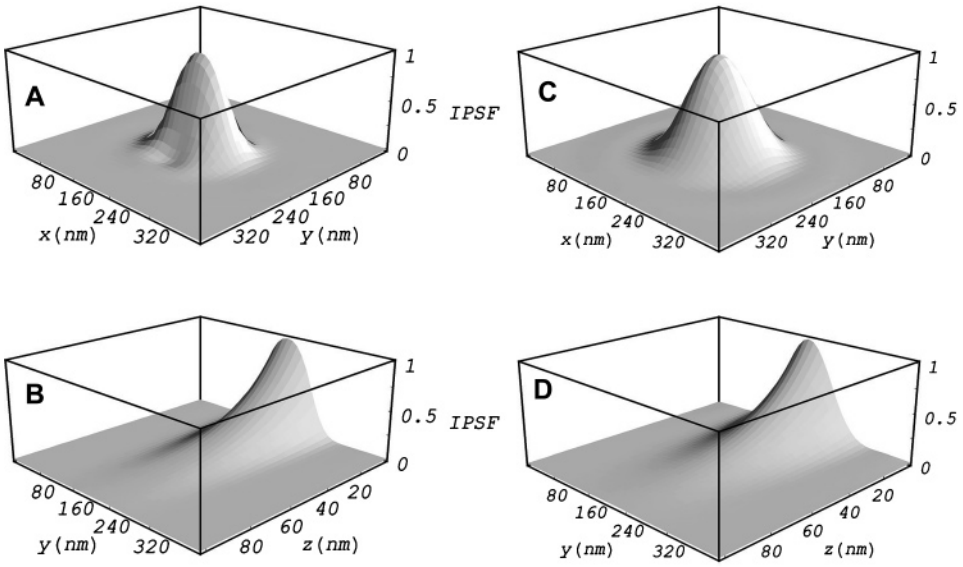

FIGURE 3: Integrated point spread functions (IPSF) for fTIRM and uTIRM. A and B contain the IPSF for the intensity distribution in Figure 2 and a 10 μm pinhole as a function of the point source position (x, y, and z). A shows IPSF for the point source constrained in the focal plane ($z = 0$). B shows IPSF for the point source constrained in an axial plane ($x = 0$). The z-dimension dependence in B is exponential with a field depth of ~100 nm. C and D contain the IPSF for uTIRM with a 5 μm pinhole and other conditions identical to that in A and B.

Table 1: Computed Detection Volumes for Various Beam Profiles

V_d (attoL)	conditions
3.1	fTIRM, 100 nm evanescent field depth, 5 μm pinhole
3.4	fTIRM, 100 nm evanescent field depth, 10 μm pinhole
6.0	fTIRM, 100 nm evanescent field depth, 25 μm pinhole
6.5	uTIRM, 100 nm evanescent field depth, 5 μm pinhole
15.2	fTIRM, 100 nm evanescent field depth, 50 μm pinhole
18.0	diffraction-limited profile, 100 nm evanescent field depth, 50 μm pinhole (hypothetical)
61.5	uTIRM, 100 nm evanescent field depth, 50 μm pinhole
104.4	uTIRM, 210 nm evanescent field depth, 50 μm pinhole

sphere. Both panels show fluorescence time traces with 1 event initiated when photon counts exceed 2 and subsequently terminated when photon counts are < 1 (see *Event Detection* in the Materials and Methods). The time per event is 10 μs in the top panel and 5 μs in the bottom panel. Time increases from left to right in Figure 5. If simulated data (bottom panel) were run backward in time, the trace would correspond to a 10 μs event. The time asymmetry is a consequence of the event detection bias that registers new events only when the detected intensity is too large to be from a noise source characterized by the average background light level. Measured and simulated data from time traces longer than those depicted in Figure 5 often had the sphere entering and leaving V_d several times while lingering in the vicinity (data not shown).

The number and fluorescence residence duration distributions, R_n and R_f, were tabulated from measured fluorescence intensity time traces of 20 and 100 nm diameter fluorescent spheres diffusing in water. Illumination mode (uTIRM or fTIRM), pinhole diameter, and evanescent field depth were varied. We computed the residence time average and variance by eq 2. Results are summarized in Table 2. Table 3 shows simulated quantities for a comparison to those in Table 2. We find that measured sphere diffusion characteristics for fTIRM with the 10 μm pinhole are fully accounted for by the simulation, consistent with the 3.4 attoL size

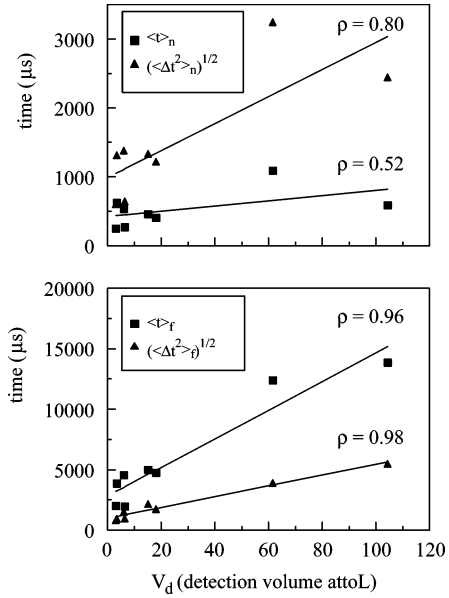

FIGURE 4: Mean (■) and rms deviation (▲) for the number- and fluorescence-intensity-residence duration distributions for 20 nm sphere-simulated diffusion. Linear regression correlation coefficients, ρ, indicate how closely two variables approximate a linear relationship to each other. Mean and rms deviation of the fluorescence-intensity-residence duration distribution is the more reliable indicator of V_d size.

estimate for V_d in Table 1. Measurement and simulation comparison for fTIRM with the 50 μm pinhole suggests that the actual V_d is somewhat smaller than the 15.2 attoL estimate in Table 1.

We did uTIRM experiments on 20 and 100 nm spheres for two evanescent field depths by using coverslips at the TIR interface with different refractive indices. The maximal field depth corresponded to a quartz coverslip with a refractive index of 1.46. The minimal field depth corresponded to the standard crown glass coverslip with a refractive index of 1.5. The excitation light incidence angle on the TIR

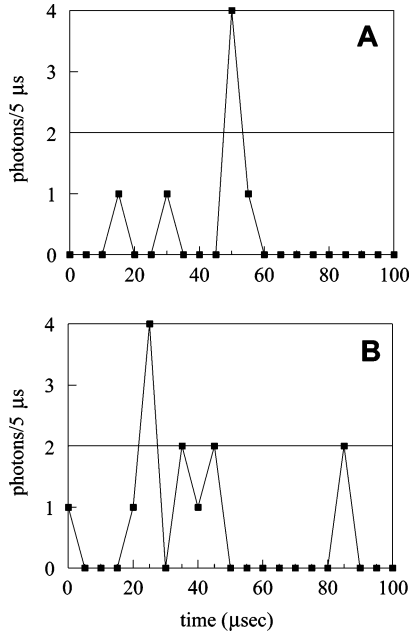

FIGURE 5: Fluorescence photon counts per 5 μs sampling time interval from a 20 nm diameter fluorescent sphere diffusing through a 3.4 attoL detection volume. Illumination is from fTIRM with a NA 1.45, 60× objective and 10 μm diameter confocal pinhole. A shows experimental data, and B shows the simulation based on the random walk diffusion model. Both A and B show fluorescence time traces with 1 event initiated when photon counts exceed 2 and subsequently terminated when photon counts are <1.

Table 2: Measured Sphere Movement Characteristics for Various Beam Profiles

	fTIRM		
field depth (nm)	invariable		
sphere size (nm)	20		100
pinhole (μm)	10	50	50
$\langle t\rangle_n/(\langle(\Delta t)^2\rangle_n)^{1/2}$ (μs)	8/5	28/52	
$\langle t\rangle_f/(\langle(\Delta t)^2\rangle_f)^{1/2}$	10/5	39/75	
	uTIRM		
field depth (nm)	maximal		minimal
sphere size (nm)	20		100
pinhole (μm)	50		50
$\langle t\rangle_n/(\langle(\Delta t)^2\rangle_n)^{1/2}$ (μs)	332/576		1950/2630
$\langle t\rangle_f/(\langle(\Delta t)^2\rangle_f)^{1/2}$	493/868		3425/3505

interface was constant at ~68°, corresponding to penetration depths of ~160 and 100 nm for quartz and glass interfaces, respectively. The quartz coverslip produced more intense fields in the water medium needed to detect the 20 nm spheres in uTIRM (the focused spot in fTIRM produces a much more intense illumination than the uTIRM uniform illumination).

The size and shape of V_d under uTIRM illumination and with the 50 μm pinhole is a cylindrically symmetric solid volume with an axial depth, defined by the evanescent field, that is much shorter than any lateral dimension. In this case, sphere diffusion characteristics are determined solely by the evanescent field depth. A comparison of sphere diffusion characteristics in Tables 2 and 3 for the 20 nm spheres (50 μm pinhole) and maximal evanescent field depth show that the observed quantities fall between the simulated values for 100 and 210 nm field depths. Sphere diffusion characteristics for the 100 nm spheres (50 μm pinhole) and minimal field depth show a good agreement with simulated values for the 100 nm field depth.

Figure 6 shows the fluorescence intensity from SH1-labeled myosin cross-bridges in a skeletal muscle fiber. The fiber was illuminated using fTIRM and a 5 μm pinhole, giving a detection volume from Table 1 of ~3 attoL. The top panel shows the raw data (green squares), baseline (black line), the stepwise fit with eight variable height steps (blue line), and the residual between the data and fit (red line) for the full time course of the experiment. The bottom panel shows the raw data for the first 20 s of the bleaching curve, where stepwise photobleaching is most clearly discernible. The data shows that most of the photobleachable light originates from five probes within the 3 attoL detection volume. For these five probes, the mean ± standard deviation step height and lifetime are 1332 ± 411 photons/s and 9 ± 6 s, giving ~12 000 photons/probe detected. The 5′-IATR is known to undergo ~10^6 excitation/relaxation cycles before photobleaching, implying that light collection efficiency was ~1% for this experiment. Step decrements are variable in height because the brightest probes, located at the interface where the evanescent field is most intense, have the highest excitation rate and are most likely to photobleach.

We simulated fluorescence intensity from probes in a lattice, imitating those on cross-bridges in a muscle fiber and resident in the detection volume appropriate for the experiment on SH1-labeled muscle fibers described above. The results obtained parallel to those shown in Figure 6 for the 3 attoL detection volume. The Supporting Information contains a description of how the simulations were performed and a summary of the results.

DISCUSSION

Fraunhofer diffraction in a clear circular aperture imaging system produces the PSF with the familiar Airy pattern and image resolution dependent upon the light wavelength and numerical aperture (*16*). The annular aperture variant is of interest in astronomical applications where the central portion of the telescope aperture is obstructed by the secondary mirror. The obstruction increases resolving power but decreases the contrast by narrowing the primary maximum while lowering the primary intensity and increasing the intensity in the side lobes. The general intensity distribution in the back aperture is the pupil function, and its manipulation to obtain a desired image intensity profile is a process called apodization. Born and Wolf briefly review the subject and the work contributing to its understanding (*16*). Lately, interest in apodization is driven by the desire to improve the resolution in microscope images, and elegant optimization methods have been described to design pupil functions in excitation and emission collection pathways to achieve desired goals for the PSF shape (*31*). Others have used apodization to alter polarization properties of the microscopic excitation field for particular applications (*32*). Manipulating the image intensity distribution by use of obstructions in the circular aperture is aptly called PSF engineering using pupil-plane filters, and the broad conclusion recently expressed is that pupil-plane filters alone cannot improve the resolution because they do not modify inherent limitations in the optical system to transfer information from the object to the image (*33*). Annular illumination in our fTIRM system is a necessity originating from the primary requirement to achieve total internal reflection. Secondary to this, we find that the resulting excitation profile defines a smaller than expected

Table 3: Simulated Sphere Movement Characteristics for Various Beam Profiles

	fTIRM					
sphere size (nm)	20				100	
field depth (nm)	100		210		100	210
pinhole (μm)	10	25	50	50	50	50
$\langle t\rangle_n/(\langle(\Delta t)^2\rangle_n)^{1/2}$ (μs)	12/11	43/62	43/67			
$\langle t\rangle_f/(\langle(\Delta t)^2\rangle_f)^{1/2}$ (μs)	14/12	72/83	78/92			
	uTIRM					
sphere size (nm)	20				100	
field depth (nm)	100		210		100	210
pinhole (μm)	10	25	50	50	50	50
$\langle t\rangle_n/(\langle(\Delta t)^2\rangle_n)^{1/2}$ (μs)			381/305	626/625	2089/2534	3226/4278
$\langle t\rangle_f/(\langle(\Delta t)^2\rangle_f)^{1/2}$ (μs)			465/325	833/668	3527/3054	5766/5117

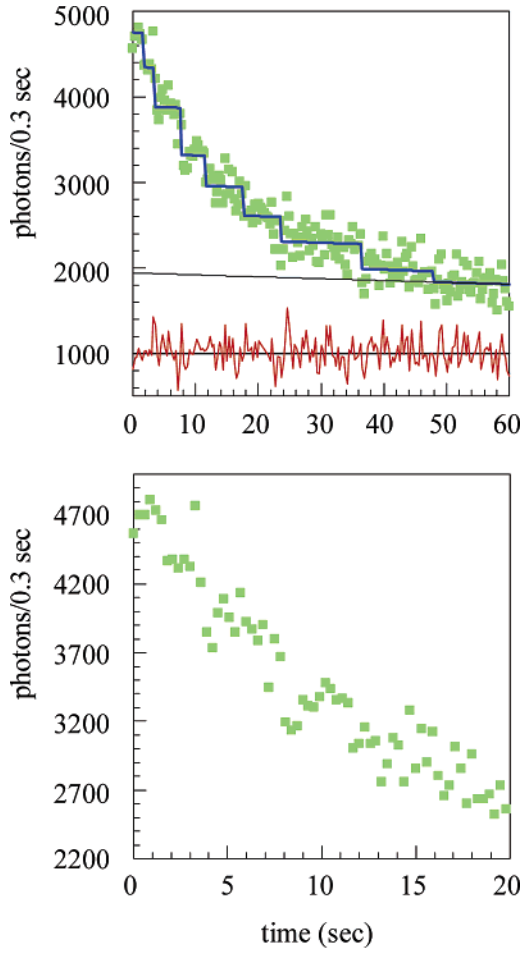

FIGURE 6: Fluorescence intensity from SH1-labeled myosin cross-bridges in a skeletal muscle fiber under fTIRM illumination producing an ~3 attoL detection volume. The top panel shows the raw data (green squares), baseline (black line), stepwise fit with eight variable height steps (blue line), and the residual between the data and fit (red line). The bottom panel shows the raw data for the first 20 s of the curve.

V_d. A smaller V_d helps achieve the experimental goal to selectively illuminate single fluorescent-labeled protein molecules in situ, where they operate in a crowded environment.

Detection volumes for a variety of uTIRM and fTIRM setups were measured using the Brownian motion of fluorescent nanospheres. To interpret fTIRM-derived data, we calculated the three-dimensional vector electric field density near the focus for a large aperture lens with an annular pupil function illuminated by a Gaussian laser beam undergoing total internal reflection at the coverslip/water interface (*34*). We used this excitation field profile to compute the IPSF and then V_d. The IPSF and V_d for uTIRM-derived data was similarly surmised for a laterally uniform excitation field profile (the profile in the axial dimension because of the evanescent field is essentially the same for uTIRM and fTIRM). Table 1 summarizes our results, where we see that the expected minimum V_d is ~3 attoL for fTIRM and ~7 attoL for uTIRM.

Next, we characterized nanosphere Brownian motion with the number- and fluorescence-intensity-residence duration distributions, R_n and R_f. Simulated data demonstrated that the mean and rms deviation of R_f, $\langle t\rangle_f$, and $(\langle\Delta t^2\rangle_f)^{1/2}$ were highly correlated with V_d, implying that they are the appropriate parameters to monitor V_d. A comparison of $\langle t\rangle_f$ and $(\langle\Delta t^2\rangle_f)^{1/2}$ from Table 2 (experimental) and Table 3 (simulated) indicated that our estimates for V_d in Table 1 are accurate. The exception was $\langle t\rangle_f$ and $(\langle\Delta t^2\rangle_f)^{1/2}$ observed from 20 nm spheres with fTIRM with the 50 μm pinhole, where the calculated 15 attoL V_d is apparently too large. We suspect that the side lobe contribution to the 15 attoL estimate does not similarly contribute to the measured value because the fluorescence intensity excited by the side lobes is too close to the background and ignored when data are processed by the event detection rules. Figure 3 shows that the side-lobe intensities are very effectively removed by use of a 10 μm pinhole. The same is true for the 25 μm pinhole (data not shown).

The combination of uTIRM and fTIRM illumination modes is an effective means for providing a comprehensive description of V_d. The size and shape of V_d under uTIRM illumination with the 50 μm pinhole is a cylindrically symmetric solid volume with an axial depth, defined by the evanescent field, that is much shorter than any lateral dimension. As such, sphere diffusion characteristics are determined solely by the evanescent field depth. Using uTIRM with the 50 μm pinhole, we showed that 100 nm is a realistic estimate for evanescent field depth.

The high concentration of myosin and other constituent proteins in the fiber suggests that the myosin function could be dramatically impacted by the effects of molecular crowding (*35*). Our work demonstrates that evanescent field illumination combined with confocal microscopy is a powerful and novel technique that succeeds in isolating fluorescence from single-probed molecules in this demanding application (*24*). Successful single-molecule detection required low myosin cross-bridge-labeling efficiency. Skeletal muscle A-bands contain ~120 μM myosin or ~72 myosins/attoL, implying that detection volumes of ~1 attoL require

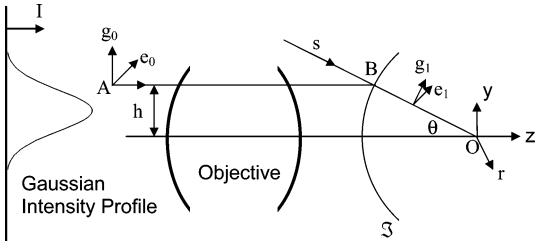

FIGURE 7: Gaussian laser beam with electric field polarization e_0 is incident on the back aperture of an objective. The light ray at height h from the optical axis is traced through the aplanatic optical system to the focal point at origin O.

<10% labeling efficiency to isolate ~7 myosins. Consequently, we detect signals from cross-bridges for which it is difficult to test in situ functionality. For instance, with ~10% of the cross-bridges labeled, 100% loss of their ATPase or contractility could be hidden by normal variability between fibers. Nevertheless, sparse probe results are probably acceptable if confirmed by several probes, at the same and/or different points on myosin. Furthermore, reliable single-molecule experiments averaged over many molecules would agree with ensemble averaged results, where labeled fractions could be close to 1. Either or both controls could be performed to affirm conclusions on myosin dynamics derived from in situ data detected from probed myosins.

Conclusion. An annular pupil filter was used to produce a focused and total internally reflecting excitation beam in a confocal fluorescence microscope. The evanescent field lateral and axial intensity profiles convoluted with emission collection intensity define a detection volume, V_d, for the instrument that can be as small as ~3 attoL. The estimate was checked experimentally by measuring characteristic times for Brownian motion of fluorescent nanospheres through V_d. The fluorescence-intensity-residence duration distribution for Brownian motion was shown to characterize V_d via the mean and rms deviation of residence times. A comparison of computed and measured values confirms V_d ~ 3 attoL. Isolation of single-labeled myosin molecules in a muscle fiber demonstrates that the technique provides the means to study protein dynamics in situ.

APPENDIX

Shape of the Excitation Field. The exciting field shape was calculated with geometrical optics for a Gaussian laser beam intensity profile at the entrance pupil of the objective by the method described previously (*34*, *36*). Figure 7 shows system elements involved after the diagram by Richards and Wolf (*34*). A light ray from the Gaussian intensity (I) profile in object space propagates parallel to and at a distance h from the optical axis (z) toward the aplanatic objective made up of several elements. The refracted ray propagates in the direction of the unit vector s making an angle θ with the optical axis that it intersects at focus O. The focal sphere $\mathcal{F}$ is centered on O and has a radius equal to the focal length, f, of the system. The electric field polarization of incident and refracted fields are e_0 and e_1, respectively. The meridional plane is the plane formed by the ray in object and image space (plane ABO). The angle formed between the meridional plane and the incident electric field, defined by vectors (g_0,e_0) and (g_1,e_1), is conserved following refraction by the objective (*34*).

The time-independent part of the electric field in image space was shown to be

$$\vec{e}(x,y,z) = \frac{-ik}{2\pi}\int_{\Omega_0} \vec{a}(s_x,s_y)\exp(ik\vec{s}\,\vec{r})\mathrm{d}\Omega \qquad \text{(A1)}$$

where k is the wavenumber in image space, r is the observation point vector in image space coordinates (x, y, and z), Ω_0 is the solid angle formed by all geometrical rays passing through the exit pupil of the objective, and vector amplitude

$$\vec{a}(s_x,s_y) = fL(x,y)\cos^{1/2}(\theta)\vec{e}_1 \qquad \text{(A2)}$$

Scalar Gaussian beam amplitude factor $L(x,y) = L_0 \exp\{-[(x - x_0)^2 + (y - y_0)^2]/w_0^2\}$ for constant L_0, and (x_0,y_0) is the beam displacement from the optical axis. The sine condition requires $h = (x^2 + y^2)^{1/2} = f \sin\theta$ (*34*). Then, $\sin\alpha = d/f$ for α, the half angle, and d, the radius of the objective aperture. Objective numerical aperture NA = $n \sin(\alpha)$, where n is the refractive index of the objective, giving $d = f\,\mathrm{NA}/n$. Let $\beta = d/w_0$, then

$$L(\theta,\phi) = L_0 \exp\left[-\left(\frac{\beta n}{\mathrm{NA}}\right)^2\left\{\left(\sin\theta\cos\phi - \frac{x_0}{f}\right)^2 + \left(\sin\theta\sin\phi - \frac{y_0}{f}\right)^2\right\}\right] \qquad \text{(A3)}$$

We derive electric field vector e_1 by following the steps outlined by Richards and Wolf (*34*).

For fTIRM, we want to know the focused field in the water side of the glass/water interface formed by the cover slip and sample. Define a meridional plane fixed coordinate frame with origin at O, with the z axis parallel to the optical axis and xz plane coplanar with the meridional plane for each ray in image space. In meridional plane coordinates, the electric field vector transmitting the interface, e^t, is

$$\begin{pmatrix} e_x^t \\ e_y^t \\ e_z^t \end{pmatrix} = \begin{pmatrix} T_p & 0 & 0 \\ 0 & T_s & 0 \\ 0 & 0 & T_p \end{pmatrix}\begin{pmatrix} e_x^i \\ e_y^i \\ e_z^i \end{pmatrix} \qquad \text{(A4)}$$

where $T_{p,s}$ values are Fresnel coefficients for fields parallel (p) or perpendicular (s) to the incidence plane and e^i is the incident electric field vector. Fresnel coefficients depend upon the angle of incidence, θ, and on the refractive indices in the glass, n_g, and water, n_w (*16*). Image space coordinates (fixed to the interface and shown in Figure 7) are referred to the meridional plane coordinates by the rotation matrix

$$m(\phi) = \begin{pmatrix} \cos\phi & \sin\phi & 0 \\ -\sin\phi & \cos\phi & 0 \\ 0 & 0 & 1 \end{pmatrix} \qquad \text{(A5)}$$

The transmitted field polarization vector in image space coordinates, e_1^t, is then derived from e_1 with

$$e_1^t = m(-\phi)\begin{pmatrix} T_p & 0 & 0 \\ 0 & T_s & 0 \\ 0 & 0 & T_p \end{pmatrix} m(\phi)e_1 \qquad \text{(A6)}$$

The propagation vector transmitting the interface in meridional coordinates is $\{\sin\theta_t, 0, \cos\theta_t\}$ for $n_w \sin\theta_t = n_g \sin\theta$

(Snell's law) and $\cos\theta_t = [1 - (n_g \sin\theta/n_w)^2]^{1/2}$. The transmitted field propagation vector in image space coordinates

$$\vec{s}^{\,t} = m(-\phi)\begin{pmatrix} \frac{n_g}{n_w}\sin\theta \\ 0 \\ \sqrt{1-\left(\frac{n_g}{n_w}\sin\theta\right)^2} \end{pmatrix} \quad \text{(A7)}$$

The transmitted field follows from eqs A1−A3 and A5−A7, such that

$$\vec{e}(x,y,z) = \frac{-ikf}{2\pi}\int_{\Omega_0} L(\theta,\phi)\cos^{1/2}(\theta)\vec{e}_1^{\,t}\exp(ikn_w\vec{s}^{\,t}\vec{r})\mathrm{d}\Omega \quad \text{(A8)}$$

SUPPORTING INFORMATION AVAILABLE

Methods and results from simulated fluorescence intensity from probes in a lattice, imitating those on cross-bridges in a muscle fiber and resident in the detection volume. This material is available free of charge via the Internet at http://pubs/acs/org.

REFERENCES

1. Neuweiler, H., and Sauer, M. (2005) Exploring life by single-molecule fluorescence spectroscopy, *Anal. Chem.* 179A−185A.
2. Dunn, R. C. (1999) Near-field scanning optical microscopy, *Chem. Rev. 99*, 2891−2927.
3. Rosenberg, S. A., Quinlan, M. E., Forkey, J. N., and Goldman, Y. E. (2005) Rotational motions of macromolecules by single-molecule fluorescence microscopy, *Acc. Chem. Res. 38*, 583−593.
4. Warshaw, D. M., Hayes, E., Gaffney, D., Lauzon, A. M., Wu, J., Kennedy, G., Trybus, K., Lowey, S., and Berger, C. (1998) Myosin conformational states determined by single fluorophore polarization, *Proc. Natl. Acad. Sci. U.S.A. 95*, 8034−8039.
5. Minton, A. P. (2001) The influence of macromolecular crowding and macromolecular confinement on biochemical reactions in physiological media, *J. Biol. Chem. 276*, 10577−10580.
6. Timasheff, S. N. (2002) Protein−solvent preferential interactions, protein hydration, and the modulation of biochemical reactions by solvent components, *Proc. Natl. Acad. Sci. U.S.A. 99*, 9721−9726.
7. Huxley, H. E. (1969) The mechanism of muscular contraction, *Science 164*, 1356−1366.
8. Huxley, A. F., and Simmons, R. M. (1971) Proposed mechanism of force generation in striated muscle, *Nature 233*, 533−538.
9. Bagshaw, C. R. (1982) in *Outline Studies of Biology: Muscle Contraction*, pp 22, Chapman and Hall, London, U.K.
10. Schrader, M., Hell, S. W., and van der Voort, H. T. M. (1998) Three-dimensional super-resolution with a 4Pi-confocal microscope using image restoration, *J. Appl. Phys. 84*, 4033−4042.
11. Klar, T. A., Jakobs, S., Dyba, M., Egner, A., and Hell, S. W. (2000) Fluorescence microscopy with diffraction resolution barrier broken by stimulated emission, *Proc. Natl. Acad. Sci. U.S.A. 97*, 8206−8210.
12. Dyba, M., Jakobs, S., and Hell, S. W. (2003) Immunofluorescence stimulated emission depletion microscopy, *Nat. Biotechnol. 21*, 1303−1304.
13. Levene, M. J., Korlach, J., Turner, S. W., Foquet, M., Craighead, H. G., and Webb, W. W. (2003) Zero-mode waveguides for single-molecule analysis at high concentrations, *Science 299*, 682−686.
14. Samiee, K. T., Foquet, M., Guo, L., Cox, E. C., and Craighead, H. G. (2005) λ-Repressor oligomerization kinetics at high concentrations using fluorescence correlation spectroscopy in zero-mode waveguides, *Biophys. J. 88*, 2145−2153.
15. Axelrod, D., Burghardt, T. P., and Thompson, N. L. (1984) Total internal reflection fluorescence, *Annu. Rev. Biophys. Bioeng. 13*, 247−268.
16. Born, M., and Wolf, E. (1975) in *Electromagnetic Theory of Propagation, Interference, and Diffraction of Light*, pp 370−458, Pergamon Press, Oxford, U.K.
17. Axelrod, D., Hellen, E. H., and Fulbright, R. M. (1992) in *Topics in Fluorescence Spectroscopy. Volume 3: Biomedical Applications* (Lakowicz, J. R., Ed.) pp 289−343, Plenum, New York.
18. Axelrod, D. (2001) Total internal reflection fluorescence microscopy in cell biology, *Traffic 2*, 764−774.
19. Ruckstuhl, T., and Seeger, S. (2004) Attoliter detection volumes by confocal total-internal-reflection fluorescence microscopy, *Opt. Lett. 29*, 569−571.
20. Ruckstuhl, T., and Seeger, S. (2003) Confocal total-internal-reflection fluorescence microscopy with a high-aperture parabolic mirror lens, *Appl. Opt. 42*, 3277−3283.
21. Ruckstuhl, T. (2005) Sometimes less is more: Parabolic optics improve analytical sensitivity, *Biophotonics 12*, 48−51.
22. Starr, T. E., and Thompson, N. L. (2002) Local diffusion and concentration of IgG near planar membranes: Measurement by total internal reflection with fluorescence correlation spectroscopy, *J. Phys. Chem. B 106*, 2365−2371.
23. Ajtai, K., Ilich, P. J. K., Ringler, A., Sedarous, S. S., Toft, D. J., and Burghardt, T. P. (1992) Stereospecific reaction of muscle fiber proteins with the 5′ or 6′ isomer of iodoacetamidetetramethyl rhodamine, *Biochemistry 31*, 12431−12440.
24. Borejdo, J., Talent, J., Akopova, I., and Burghardt, T. P. (2006) Rotations of a few cross-bridges in muscle by confocal total internal reflection microscopy, *Biochim. Biophys. Acta*, in press.
25. Borejdo, J., Putnam, S., and Morales, M. F. (1979) Fluctuations in polarized fluorescence: Evidence that muscle cross bridges rotate repetitively during contraction, *Proc. Natl. Acad. Sci. U.S.A. 76*, 6346−6350.
26. Ajtai, K., and Burghardt, T. P. (1989) Fluorescent modification and orientation of myosin sulfhydryl 2 in skeletal muscle fibers, *Biochemistry 28*, 2204−2210.
27. Burghardt, T. P., Garamszegi, S. P., and Ajtai, K. (1997) Probes bound to myosin Cys-707 rotate during length transients in contraction, *Proc. Natl. Acad. Sci. U.S.A. 94*, 9631−9636.
28. Berg, H. C. (1983) *Random Walks in Biology*, Princeton University Press, Princeton, NJ.
29. Hillesheim, L. N., and Müller, J. D. (2003) The photon counting histogram in fluorescence fluctuation spectroscopy with non-ideal photodetectors, *Bioophys. J. 85*, 1948−1958.
30. Wilson, T. (1990) in *Confocal Microscopy* (Wilson, T., Ed.) pp 1−64, Academic Press, New York.
31. Neil, M. A. A., Juškaitis, R., Wilson, T., Laczik, Z. J., and Sarafis, V. (2000) Optimized pupil-plane filters for confocal microscope point-spread function engineering, *Opt. Lett. 25*, 245−247.
32. Sick, B., Hecht, B., and Novotny, L. (2000) Orientational imaging of single molecules by annular illumination, *Phys. Rev. Lett. 85*, 4482−4485.
33. Davis, B. J., Karl, W. C., Swan, A. K., and Ünlü, M. S. (2004) Capabilities and limitations of pupil-plane filters for superresolution and image enhancement, *Optics Express 12*, 4150−4156.
34. Richards, B., and Wolf, E. (1959) Electromagnetic diffraction in optical systems. II. Structure of the image field in an aplanatic system, *Proc. R. Soc. London, Ser. A 253*, 358−379.
35. Muhlrad, A., Peyser, Y. M., Nili, M., Ajtai, K., Reisler, E., and Burghardt, T. P. (2003) Chemical decoupling of ATPase activation and force production from the contractile cycle in myosin by steric hindrance of lever arm movement, *Biophys. J. 84*, 1047−1056.
36. Yoshida, A., and Asakura, T. (1974) Electromagnetic field near the focus of Gaussian beams, *Optik 41*, 281−292.

BI052097D